Journal of Materials Chemistry A

ROYAL SOCIETY OF CHEMISTRY

PAPER

View Article Online
View Journal

Cite this: DOI: 10.1039/d6ta02016j

Orbital overlap-stabilized amorphous metal phosphate frameworks for industrial current density electrocatalysis

Jinyan Xie,[ab] Shiyu Yang,[ab] Ziyong Zhang,[ac] Fei Han,[a] Ruizhe Ru,[ab] Lei Zhang,[a] Zunming Lu,[c] Guowei Li,*[a] Jun-Qiang Wang*[ab] and Juntao Huo*[ab]

Transition-metal phosphates are promising catalysts for water splitting owing to their high density of active sites and open framework that facilitates rapid ion diffusion. However, lattice-oxygen-induced phosphate leaching and the weak, variable M–O covalency often lead to surface reconstruction and performance degradation at high current densities. Here, we address these challenges by constructing an amorphous phosphate surface layer (Ru2-De) through a minor Ru alloying strategy combined with *in situ* amorphization of an FeCoNiRuP precursor. The incorporation of Ru induces strong Ru 4d–O 2p hybridization, which enhances orbital overlap and M–O covalency, effectively suppressing phosphate framework dissolution. Simultaneously, the increased density of states near the Fermi level and narrowed band gap improve charge transport. As a result, Ru2-De exhibits excellent catalytic activity with overpotentials of 23 mV for the hydrogen evolution reaction (HER) and 257 mV for the oxygen evolution reaction (OER) at 10 mA cm^{-2}. Notably, when employed simultaneously as both the cathode and anode in an anion-exchange membrane (AEM) electrolyzer at 80 °C, the system exhibits high efficiency, requiring only 1.61 V to reach 500 mA cm^{-2}, while retaining exceptional durability for over 100 h at 1 A cm^{-2}. These metrics place Ru2-De among benchmark catalysts for high-current-density water electrolysis. Such a low-Ru, scalable platform provides an effective strategy to suppress structural collapse and active-site degradation at high current densities, offering a robust pathway toward industrially durable water electrolysis.

Received 8th March 2026
Accepted 20th April 2026

DOI: 10.1039/d6ta02016j

rsc.li/materials-a

Introduction

The development of efficient and durable electrocatalysts capable of operating at high current densities is critically important for advancing large-scale hydrogen production.[1–3] In practical applications, industrial alkaline electrolyzers typically demand current densities above 500 mA cm^{-2},[4] while proton exchange membrane systems can reach the ampere-level.[5–8] Achieving such operational conditions, however, imposes tremendous mechanical, thermal, and electrochemical stress on catalysts, leading to the problems of active-site degradation,[9] over-oxidation,[10] and structural collapse,[11,12] all of which lead to a rapid decay in performance.[13] Thus, the design of robust catalysts that retain high activity and structural integrity at extreme current densities remains a central challenge in sustainable hydrogen production.[14,15] Recent reviews on metal selenides for electrocatalytic H_2 evolution have highlighted similar challenges in developing robust non-precious metal catalysts, underscoring the urgent need for innovative structural design strategies.[16]

Among the various families of non-precious metal catalysts, transition-metal phosphates (TMPs) have emerged as promising candidates due to their unique combination of crystal and electronic characteristics.[17–19] The incorporation of phosphate anions (PO_4^{3-}) not only stabilizes the metal center through strong metal–oxygen–phosphate (M–O–P) linkages, but also provides open frameworks that facilitate ion and electron transport.[20–22] The phosphate groups can effectively modulate the electronic configuration of transition metals, optimize intermediate adsorption energies, and mitigate surface oxidation, which together enhance both activity and durability.[23] Moreover, TMPs offer chemical tunability through compositional variation (Fe, Co, Ni, Mn, *etc.*), enabling precise control over redox behavior and catalytic kinetics.[24,25] Recent advances in heterojunction engineering demonstrate the critical role of interfacial design: MXene charge bridges enable fast carrier transport,[26] black phosphorus/$CoNiSe_2$ and Ni_2P/black

[a]Zhejiang Key Laboratory of Magnetic Materials and Applications, Ningbo Institute of Materials Technology and Engineering, Chinese Academy of Science, Ningbo, Zhejiang 315201, China. E-mail: liguowei@nimte.ac.cn; jqwang@nimte.ac.cn; huojuntao@nimte.ac.cn

[b]Center of Materials Science and Optoelectronics Engineering, University of Chinese Academy of Sciences, Beijing, 100049, China

[c]School of Materials Science and Engineering, Hebei University of Technology, Tianjin 300130, China

phosphorus heterojunctions with built-in electric fields enhance AEM electrolysis performance,[4,27] vacancy-rich $NiCo_2O_4$/NiCoP heterojunctions improve alkaline water splitting,[28] and Ti–S bonded NiS_2/Ti_3CNCl_2 MXene heterojunctions[29] boost OER activity.

Despite these advantages, conventional crystalline TMPs still face intrinsic limitations that hinder their application at high current densities.[18] During prolonged operation, the lattice-oxygen mechanism often activates lattice oxygen participation in the oxygen evolution reaction (OER), leading to phosphate leaching and surface amorphization. This process weakens the M–O covalency, destroys the local coordination environment, and causes continuous surface reconstruction, resulting in a decline of catalytic activity and mechanical integrity.[30–32] Additionally, the rigid crystalline framework restricts atomic rearrangement during the reaction, creating stress accumulation and particle cracking under rapid redox cycling.[33,34] The coupled effects of chemical leaching and mechanical stress ultimately lead to structural collapse,[35] active-site loss,[10] and performance degradation under industrially relevant conditions.[36]

A promising route to overcome these challenges is to construct amorphous transition-metal phosphates (a-TMPs). The absence of long-range atomic order in amorphous materials provides remarkable structural flexibility, allowing them to tolerate local distortions and accommodate large volume changes during redox processes.[37,38] This structural adaptability effectively minimizes mechanical stress and prevents crack formation, thereby improving long-term stability.[39] Furthermore, the disordered atomic arrangement provides highly active centers for catalytic reactions.[40] The continuous distribution of bond lengths and angles allows dynamic adjustment of adsorption energies, promoting favorable reaction pathways and reducing activation barriers.[41–43] Most importantly, unlike crystalline materials constrained by symmetry and fixed lattice sites, amorphous matrices allow high dopant solubility without inducing phase segregation or lattice strain.[44] This makes it possible to introduce heteroatoms that modulate M–O covalency, enhance electronic conductivity, and stabilize surface oxygen species.[45] In particular, doping with 4d or 5d transition metals, such as Ru, Mo, or W, can significantly alter the electronic structure by introducing extended d orbitals that hybridize strongly with O 2p states,[46] thereby improving both catalytic activity and durability.

In this work, we develop a Ru minor alloying plus *in situ* amorphisation strategy to design high-performance transition-metal phosphate catalysts capable of operating at high current densities. By electrochemically dealloying FeCoNi-based metallic glass, we generate an amorphous phosphate skin (Ru2-De) with uniformly dispersed trace Ru ($\approx$2 at%). The incorporation of Ru 4d orbitals enhances Ru–O–M orbital overlap, strengthens M–O covalency, and suppresses phosphate leaching, while also increasing the density of states near the Fermi level to facilitate charge transport. This synergistic modulation of structure and electronic configuration enables Ru2-De to achieve industrial-level hydrogen evolution reaction (HER) and OER performance with outstanding long-term stability.

Results and discussion

Before entering the experimental section, we first discuss the mechanism of structural collapse and active-site degradation at high current densities of metal phosphates. Taking the OER as an example, the reaction generally proceeds *via* either the lattice-oxygen mechanism or the adsorbate-evolution mechanism (Fig. 1a). In the lattice-oxygen mechanism pathway, lattice oxygen directly participates in O–O bond formation, creating oxygen vacancies that weaken the M–O–P framework (Fig. 1b) and trigger phosphate leaching. In the adsorbate-evolution mechanism pathway, although lattice oxygen remains intact, the high oxidation potentials lead to over-oxidized metal centers (Fig. 1b),[47] bond-stress accumulation,[48] and structural fatigue.[49] Both mechanisms eventually destabilize the catalyst, causing loss of active sites and structural collapse. The fundamental origin of this instability lies in the weak M–O covalency within the open phosphate lattice, where insufficient orbital overlap renders the framework vulnerable to dissolution.

Enhancing the M–O bond strength is therefore crucial for achieving long-term stability, which can be quantified by a more negative integrated crystal orbital Hamilton population (ICOHP).[50,51] While 3d transition metals such as Fe, Co, and Ni offer good redox flexibility, their compact orbitals provide limited overlap with O 2p states. Incorporating 4d elements like Ru, with more spatially extended orbitals, significantly enhances d–p hybridization and reduces the ICOHP value, resulting in stronger and more covalent M–O bonds (Fig. 1c). The Ru 4d–O 2p hybridization broadens the electronic bandwidth, reduces antibonding occupancy near the Fermi level, and buffers over-oxidation of neighboring 3d sites, effectively suppressing both lattice-oxygen mechanism-induced phosphate leaching and adsorbate-evolution mechanism-related structural fatigue.[52]

To validate the above hypothesis, a series of $Fe_{60-x}Co_{10}Ni_{10}P_{20}Ru_x$ (x = 0, 1, 2, 3; denoted as Ru0, Ru1, Ru2, and Ru3) amorphous alloy precursors were synthesized by single-roll rapid quenching technology (Fig. 2a). These ribbons were subsequently subjected to electrochemical dealloying treatment in 2 M H_2SO_4 to generate the active catalytic surface (detailed dealloying conditions can be seen in Fig. S1). The X-ray diffraction (XRD) patterns of all samples, both before and after dealloying, exhibit only a broad diffraction peak (Fig. S1). The X-ray diffraction (XRD) patterns of all samples, both before and after dealloying, exhibit only a broad diffraction peak at 45° without any sharp peaks, indicating their amorphous nature (Fig. 2b and S2). Furthermore, high-angle annular dark-field (HAADF)-STEM images showed no evidence of cluster formation or element aggregation, while the high-resolution transmission electron microscopy (HRTEM) and selected area electron diffraction (SAED) results displayed no lattice fringes and a diffuse halo pattern (Fig. 2c and d), further confirming the amorphous nature of the dealloyed surface layer.

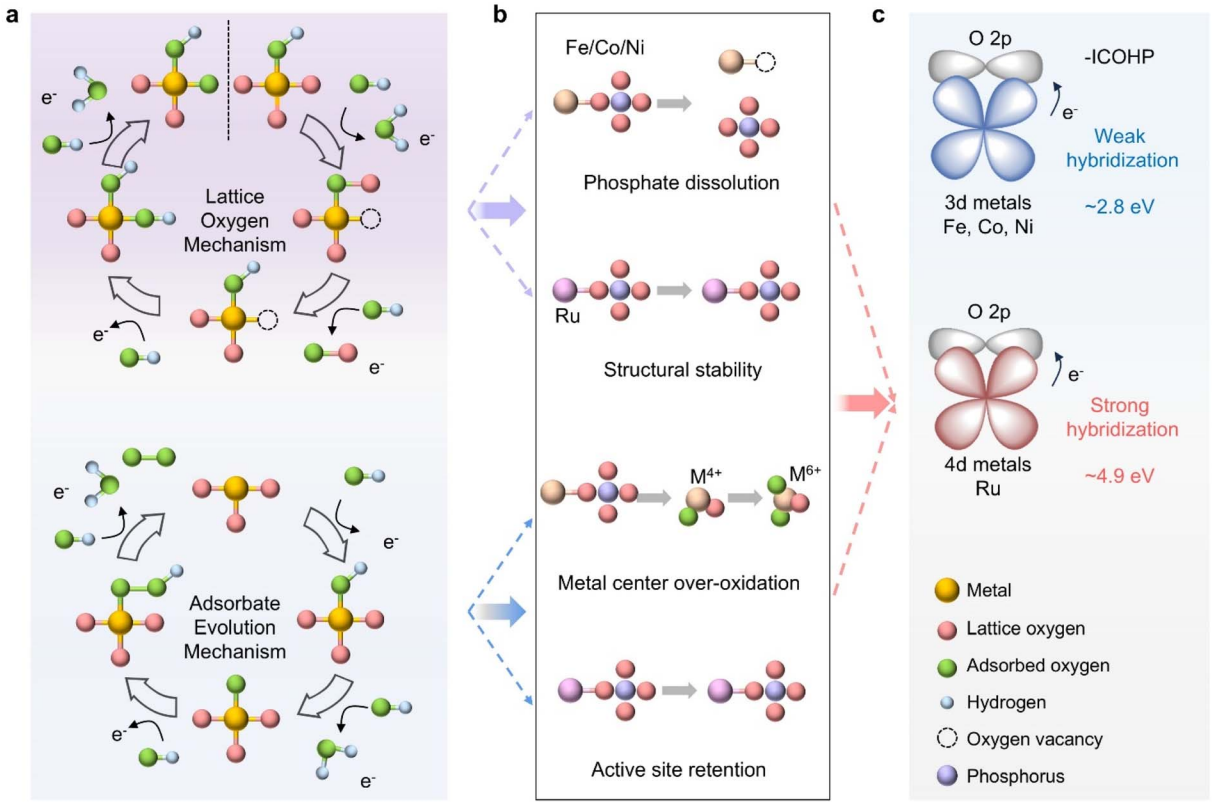

long-term stability.[39] Furthermore, the disordered atomic

Fig. 1 The design concept of 4d metal Ru-doped transition metal phosphate OER catalysts. (a) Lattice-oxygen mechanism and adsorbate-evolution mechanism of the OER. (b) Causes of deactivation of 3d transition metal phosphate catalysts under two mechanisms. (c) Revealing the mechanism by which 4d metal Ru alloying affects catalyst stability.

Based on this, we compared the amorphous states of the samples before and after dealloying treatment (Fig. S3). Before dealloying, the HRTEM image shows maze-like contrast features characteristic of amorphous structures and the SAED pattern exhibits double-ring diffraction, indicating the presence of medium-range order (MRO). After dealloying, the HRTEM contrast becomes uniform and blurred and the SAED pattern transforms into a single ring, demonstrating that the introduction of oxygen disrupts the medium-range order, resulting in a more homogeneous disordered structure. After dealloying, scanning electron microscopy (SEM) images showed that the surface of the metallic glass (MG) ribbons developed pitting pits and crack features, which became more pronounced with longer dealloying times (Fig. S4). Such surface evolution is a typical phenomenon in the dealloying of MG containing a 20 at% P element.[53] However, such defects can be significantly suppressed upon Ru incorporation, suggesting that Ru enhances surface stability during dealloying. The cross-sectional microstructure of the dealloyed sample was further examined using SEM (Fig. 2e). In the Ru2-De sample (dealloyed for 60 s), a clear 3.4 μm dealloyed layer was observed atop the MG matrix. Elemental mapping revealed a substantial decrease in Fe content (from 57.43 to 27.94 at%) and enrichment of P and Ru (from 18.60 and 2.31 to 42.91 and 6.26 at%, respectively) in the surface layer (Fig. 2f). The increased oxygen content indicates the formation of metal phosphates. Top-surface analysis confirmed the uniform dispersion of Fe, Co, Ni, P, Ru, and O (Fig. S5).

The chemical states of the metal elements and the formation of phosphate groups were analyzed by X-ray photoelectron spectroscopy (XPS) (Fig. S6 and S7). The survey spectra confirmed the presence of Fe, Co, Ni, P, and O in the Ru0 sample (Fig. S6a), while additional Ru signals appeared in the Ru2 sample (Fig. S7a), indicating the successful doping of Ru. In the Ru0 precursor, the transition metals primarily existed in zero-valent metallic states before dealloying and were partially oxidized to their corresponding metal phosphides after treatment (Fig. S6b–f). This is further confirmed by the P 2p spectrum (Fig. 2g), where the binding energy near 129.0 eV can be attributed to metal-P bonds such as FeP and CoP.[54,55] For the Ru2 sample, the XPS spectra revealed a clear transition of Fe, Co, Ni, and Ru from zero-valent states to higher oxidation states after dealloying, as evidenced by the weakening or disappearance of the metallic peaks (Fig. S7b–f). Simultaneously, the P 2p spectrum displayed only P–O bonding features (Fig. 2g), and a clear M–O signal peak can be indexed at 525.9 eV (Fig. 2h), confirming the formation of metal phosphates. This transformation results from the electrochemical dealloying process, which disrupts metallic bonding, promotes oxidation, and facilitates electron transfer from metals to phosphate groups.

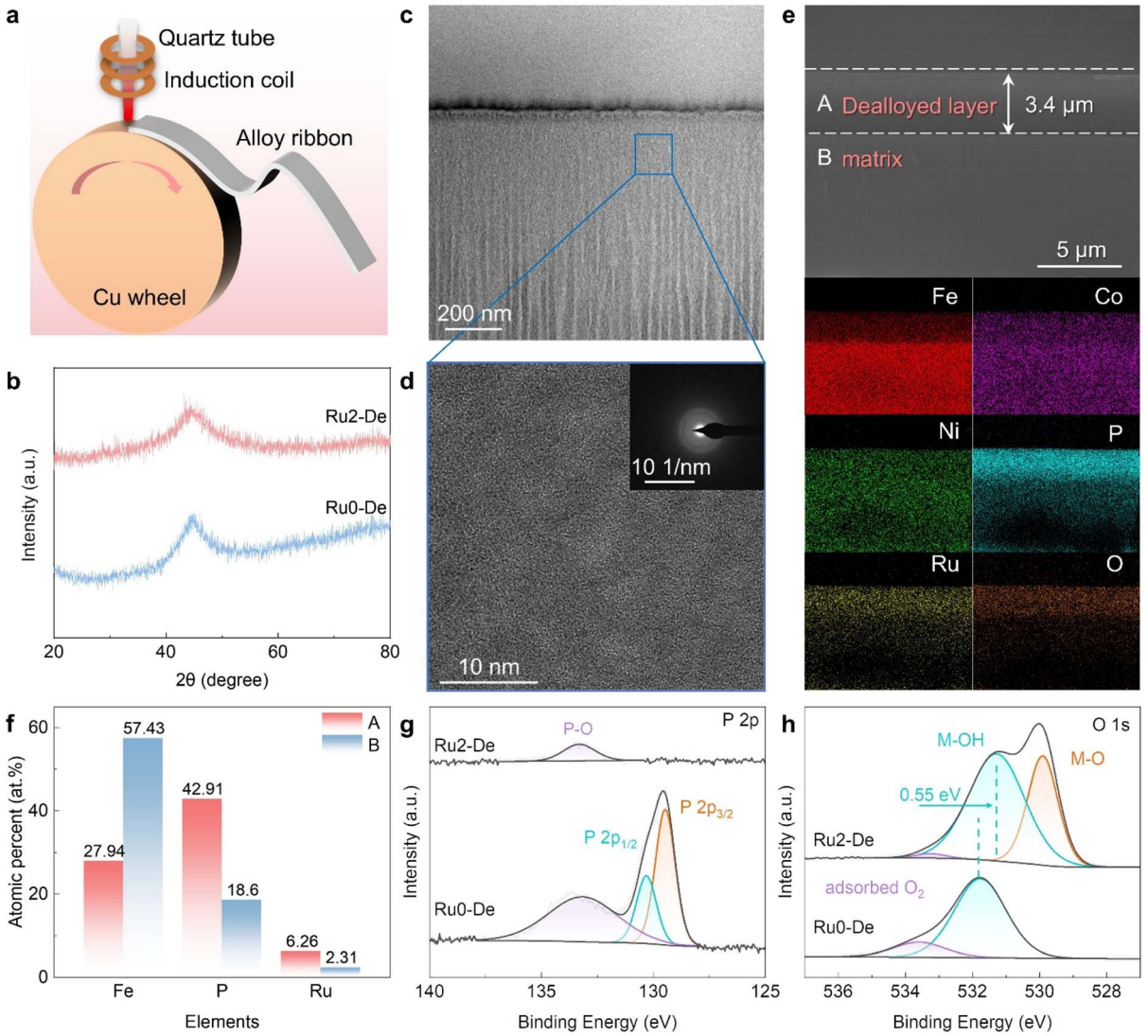

Fig. 2 (a) Preparing the samples using the single-roll rapid quenching technology. (b–e) Morphological and structural characterization. (b) XRD patterns of Ru0-De and Ru2-De. (c) STEM images of Ru2-De. (d) HRTEM images and SAED patterns of Ru2-De. (e) Cross-sectional SEM images and energy dispersive spectroscopy (EDS) mapping of Ru2-De. (f) Comparison of Fe, P, and Ru elemental contents at A and B sites in the cross-section of Ru2-De. Comparison of high-resolution (g) P 2p and (h) O 1s XPS spectra of Ru0-De and Ru2-De.

Collectively, these results demonstrate that Ru incorporation promotes the formation of a stable amorphous metal-phosphate framework, enhancing both chemical robustness and structural homogeneity.

The prepared MG strips were directly used as working electrodes to study their catalytic performance in 1 M KOH solution (experimental details can be seen in the SI). For all the samples including Ru0, Ru1, Ru2, and Ru3, dealloying treatment will significantly boost the HER activities (Fig. S8). However, over dealloying will deteriorate the activities due to the loss of self-supporting ability. Fig. 3a and S9 summarize the linear sweep voltammetry (LSV) curves of the MG strips after dealloying treatment (Fig. S10 shows the data before and after IR compensation). At a current density of 10 mA cm^{-2}, the overpotential of the Ru-introduced samples (Ru2) decreased from 299 mV to 23 mV after treatment, which is comparable to that of the commercial 20% Pt/C electrode (20 mV) and much lower than that of Ru0 (the overpotential of Ru0 before and after acid treatment was 353 mV and 104 mV, respectively) (Fig. S11). The introduction of Ru significantly improved the HER activity of the Ru0 electrode, indicating that Ru provides the main active center for the HER. In addition, the Tafel slope of the electrocatalyst was analyzed to determine the reaction mechanism (Fig. 3b). The Tafel slope of the Ru2-De electrode is the lowest at 30.74 mV dec^{-1}, much lower than those of Pt/C (44.62 mV dec^{-1}), Ru2 (92.70 mV dec^{-1}), Ru0 (85.31 mV dec^{-1}), Ru0-De (81.38 mV dec^{-1}), and nickel foam (NF) (136.03 mV dec^{-1}). The Tafel slope value of the Ru2-De electrode reveals that the rate-determining step (RDS) of the reaction is the Tafel step ($2H_{ads} \rightarrow H_2$).[56] The Ru2-De catalyst prepared in this paper has superior overpotential and Tafel slope compared to most other previously used catalysts at a current density of 10 mA cm^{-2}

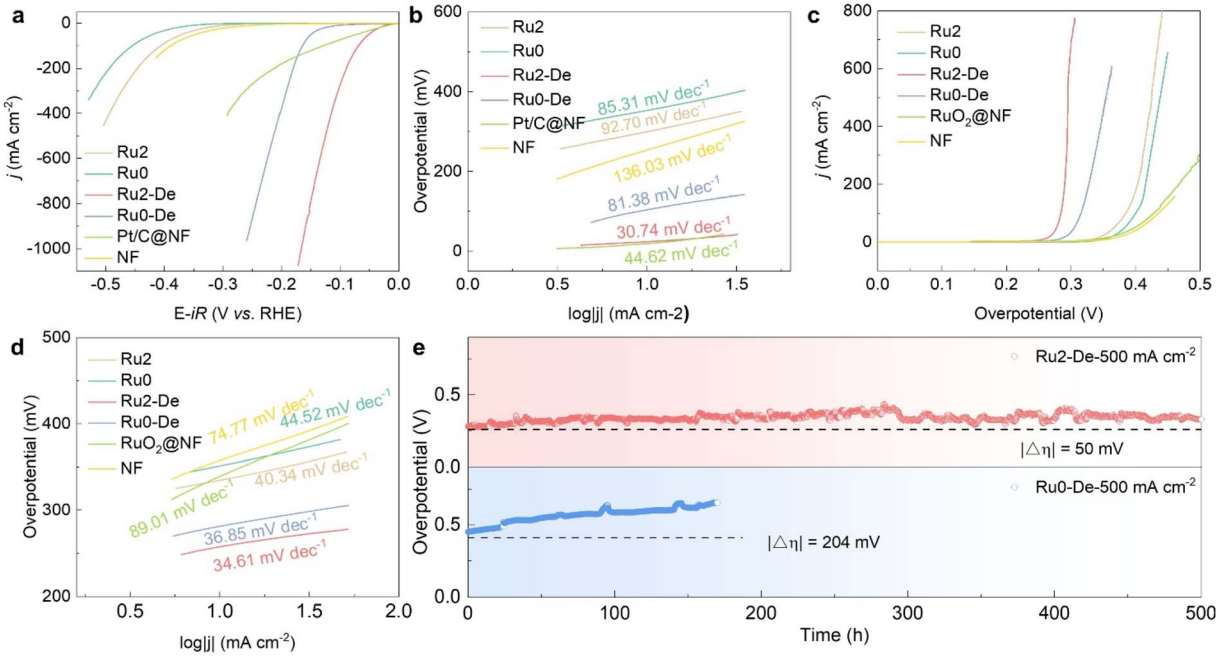

Fig. 3 Electrocatalytic hydrogen evolution and oxygen evolution reactions in 1 M KOH. (a) HER polarization curves recorded on different catalysts. (b) Corresponding Tafel plots. (c) OER polarization curves recorded on different catalysts. (d) Corresponding Tafel plots. (e) Long-term stability tests of Ru0-De and Ru2-De electrodes at the anode at a constant current density of 500 mA cm^{-2}.

(Fig. S12 and Table S1). In addition, electrochemical impedance spectroscopy (EIS) was used to evaluate the charge transfer ability of the catalyst, and the Ru2-De strip with the smallest diameter of 0.7087 Ω showed the strongest charge transfer ability compared to the other samples (Fig. S13 and S14), which is beneficial for the electrochemical HER.

To further explore the catalytic active sites of the four alloys, we measured the double-layer capacitance (C_{dl}) of Ru2 and Ru0 by cyclic voltammetry (CV) (Fig. S15 and S16), then calculated the electrochemical active surface area (ECSA) (Fig. S17), and finally determined the intrinsic activity through the turnover frequency (TOF) (Fig. S18). The calculation results showed that the C_{dl} values of Ru2, Ru0, Ru2-De, and Ru0-De were 0.12, 0.03, 3.03, and 55.46 mF cm^{-2}, respectively, corresponding to ECSA values of 3, 0.75, 75.75, and 1386.5 cm^2 for Ru2, Ru0, Ru2-De, and Ru0-De, respectively. By normalizing the polarization curves using ECSA (Fig. S19), it was found that Ru2-De is far superior to Du0-De and it was found that Ru2-De significantly outperformed Ru0-De. Meanwhile, the TOF results indicated that Ru2-De exhibited the optimal intrinsic activity, with values of 1.12H_2 s^{-1} and 3.25H_2 s^{-1} at overpotentials of 100 mV and 150 mV, respectively. This suggests that although the actual specific surface area of Ru0-De is much larger than that of Ru2-De due to the appearance of a large number of pitting pits on the surface, the actual activity of the active sites is inferior to that of Ru2-De due to the absence of Ru active medium participation. When comparing Ru2-De with recently reported advanced catalysts, it similarly demonstrated excellent performance (Fig. S20 and Table S2).

More importantly, Ru2-De has excellent cycling stability, with little change in performance after 5000 CV cycles (Fig. S21). To meet industrial application conditions, Ru2-De exhibits stable HER activity for 1000 hours of continuous testing at a high current density of 500 mA cm^{-2} (Fig. S22), while Ru0-De shows significant decay after only 240 hours of constant current testing. Comparing the stability of Ru2-De with other materials, it demonstrates excellent high-current stability and performance advantages (Fig. S23 and Table S3).

Furthermore, the oxygen evolution performance of Ru2-De in 1 M KOH was tested in a standard three-electrode system and compared with that of Ru2, Ru0, Ru0-De, and commercial RuO_2. The LSV curves of samples with different Ru contents are shown in Fig. S24 and 3c displays the polarization curves of Ru2, Ru2-De, Ru0, Ru0-De, and commercial RuO_2 with NF (Fig. S25 shows the data before and after IR compensation). Ru2-De exhibits the smallest overpotential η_{10} (257 mV), which is much lower than the values of Ru2 (334 mV), Ru0 (352 mV), Ru0-De (281 mV), and commercial RuO_2 (339 mV). As shown in Fig. 3d, the corresponding Tafel slopes of Ru2, Ru2-De, Ru0, Ru0-De, and commercial RuO_2 with NF are 44.52, 34.61, 40.34, 36.85, 89.01, and 74.77 mV dec^{-1}, respectively. To understand the mechanism of the above performance, we evaluated the charge/mass transfer at the interface. The Nyquist plots of the four materials were plotted at 0.556 V (Fig. S26). Ru2-De has the smallest charge transfer resistance of 1.266 Ω (Fig. S27), which means that the OER kinetics are much faster on Ru2-De, indicating that the Ru-doped phosphate *in situ* formed during the dealloying process promotes the transfer of electrons throughout the material.

The key parameters of our catalyst for the OER were compared with those of other recently reported noble and non-noble metal catalysts in the literature. It is encouraging to note

that the Ru2-De catalyst exhibits superior performance, characterized by a lower overpotential and a smaller Tafel slope, compared to previously reported catalysts in alkaline solutions (Fig. S28 and Table S4). Furthermore, Ru2-De showed an increase in performance after a long-term stability test of 500 hours, whereas Ru0-De experienced a 204 mV increase in overpotential after only 170 hours, representing a 45% decay from its initial state of 453 mV (Fig. 3e).

Based on the excellent HER and OER performance of Ru2-De, a two-electrode overall water-splitting device was assembled using Ru2-De as both the anode and cathode in 1.0 M KOH solution (Fig. 4a). As shown in Fig. 4b, the Ru2-De (+, −) configuration displayed a remarkably low cell voltage of 1.53 V and 1.7 V of 10 mA cm^{-2} and 500 mA cm^{-2} ($\eta_{10} = 300$ mV; $\eta_{500} = 470$ mV), significantly lower than the 376 mV and approximately 770 mV required for the Pt/C||RuO_2 system at the corresponding current densities. Meanwhile, Ru2-De demonstrated exceptional durability, retaining stable operation for over 500 hours at a high current density of 500 mA cm^{-2} without noticeable degradation (Fig. 4c). In addition, the system exhibited a faradaic efficiency close to 100% (Fig. 4d and S29), confirming nearly complete conversion of charge into hydrogen and oxygen. We compared the performance of Ru2-De at 500 mA cm^{-2} with that of similar transition metal catalysts, and the results show that this performance ranks among that of the most efficient bifunctional catalysts reported to date (Fig. 4e and Table S5). This long-term stability is in sharp contrast to that of the Ru0-De electrode, which exhibited a rapid voltage increase of 488 mV after only 220 hours of continuous operation. The overall water-splitting electrocatalytic performance of Ru2-De was further evaluated in an anion-exchange membrane (AEM) electrolyzer (active area: 1 cm^2). As shown in Fig. 4f–h, Ru2-De (+, −) achieved a current density of 500 mA cm^{-2} at 1.61 V, lower than the 1.75 V required for Ru0-De (+, −). In the AEMWE device (Ru2-De (+, −), $T = 80$ °C, 30% KOH), excellent stability was observed, retaining a current density of 1000 mA

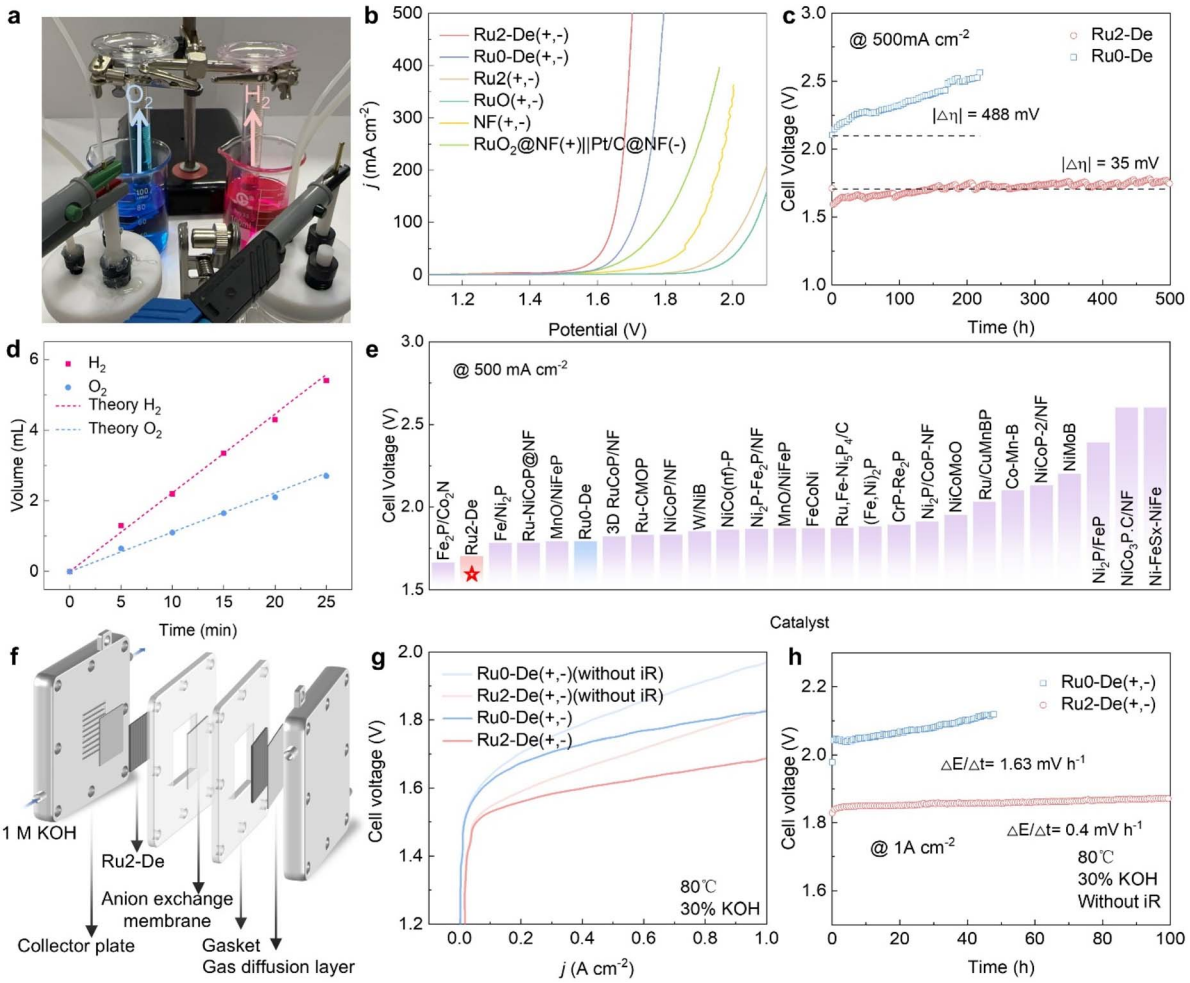

Fig. 4 The overall water-splitting reaction in 1 M KOH. (a) Photo of a self-made device for measuring the gaseous products produced by the Ru2-De (+, −) electrolyzer (Ru2-De simultaneously serves as both the anode and the cathode). (b) Polarization curve in 1 M KOH. (c) Durability test conducted in 1 M KOH at a constant current density of 500 mA cm^{-2}. (d) Comparison between the amount of gaseous products (H_2 and O_2) collected using a two-electrode electrolyzer and the theoretical amount of gaseous products in 1 M KOH at a constant current of 32 mA. (e) Comparison of cell voltage with other catalysts at 500 mA cm^{-2}. (f) Schematic of an AEMWE device. (g) LSV curve of the Ru2-De (+, −) AEMWE compared to Ru0-De (+, −). (h) Chrono-potentiometry curve of the Ru2-De (+, −) AEMWE at 1000 mA cm^{-2}.

cm^{-2} over 100 h of continuous operation with a voltage fluctuation of only 0.4 mV h^{-1}. This indicates that the Ru2-De catalyst exhibits good catalytic activity and stability during alkaline water splitting, highlighting its significant potential for large-scale hydrogen production from water electrolysis.

The impressive water electrolysis performance of Ru2-De prompts comparison with recent advances in transition-metal phosphate- and phosphide-based catalysts. Self-supported nickel–iron phosphosulfide nanotubes with engineered heterointerfaces have demonstrated impressive activity for high-current-density saline water electrolysis, achieving 67 mV overpotential at 10 mA cm^{-2} and stable operation for 100 hours.[57] Meanwhile, sulfur/phosphorus co-doped high-entropy alloys have shown promise for seawater splitting through electronic structure modulation, enabling the development of self-powered asymmetric electrolysis systems.[58] While these advances primarily utilize morphological engineering and heterostructure construction, Ru2-De achieves comparable performance through amorphous phosphate framework stabilization with trace Ru incorporation, enabling high durability at industrial current densities.

The enhanced electrochemical durability of Ru2-De is closely correlated with its improved structural stability. To reveal the origin of this stability, the electrolyte was extracted after performing oxygen evolution reaction (OER) tests at a constant current density of 500 mA cm^{-2} for 2 days and 4 days, and the dissolution amounts of transition metals and phosphorus in the electrolyte were measured (Fig. S30 and S31). After four days, the phosphorus concentration in the electrolyte of the Ru2-De system decreased markedly from 0.809 mg L^{-1} to 0.224 mg L^{-1}, indicating that Ru doping significantly suppresses phosphate leaching. Similar trends were observed for the dissolved Fe, Co, and Ni, all of which showed substantial reductions compared to the undoped sample. Cross-sectional analysis of the electrodes after stability testing (Fig. S32 and S33) further confirmed these findings. The dealloyed layer of Ru0-De became noticeably thicker, accompanied by a reduced MG core and weakened mechanical integrity (Fig. S34). In contrast, the Ru2-De electrode retained a well-defined interface and stable morphology. EDS analysis revealed that the surface O content of Ru0-De increased from 43.44 to 62.59 at%, while P decreased from 24.97 to 10.64 at%, confirming severe phosphate loss. Conversely, Ru2-De exhibited negligible changes in surface O and P content, demonstrating that Ru incorporation effectively stabilizes the amorphous phosphate framework during prolonged high-current operation. To meet industrial requirements, we conducted OER stability tests using a 30% KOH solution to verify the ICP-OES results (Fig. S35), showing a trend consistent with before: the dissolution rate of Ru2-De gradually decreases, while Ru0-De exhibits linear dissolution.

At the same time, we also observed the surface morphology after a long-term HER test at a constant current density of 500 mA cm^{-2} (Fig. S36). After 240 hours, the alloy-depleted layer with pitting corrosion on the Ru0-De surface had basically disappeared, while on the Ru2-De surface, many nanosheet-like structures appeared after 1000 hours of testing. It is precisely the formation of these numerous sheet-like structures that prevented further corrosion on the catalyst surface and preserved the internal structure. The TEM results after stability testing show that the sample still retains an amorphous state and intact structure (Fig. S37 and S38). XPS data show that after the long-term OER, the Ru 3d, O 1s, and P 2p spectra remain basically unchanged, indicating that Ru remains stable in the Ru–O–P environment and that the phosphate framework is well preserved. The slight shift in the M–O/P–O components suggests enhanced covalency and improved framework stability. After the long-term HER, the Ru 3d signal weakens, accompanied by a decrease in M–O and partial reduction of P species, indicating adaptive surface reconstruction, tending toward a phosphate/phosphide-like environment, which helps stabilize Ru and inhibit its aggregation (Fig. S39).

In situ Raman spectroscopy shows that under anodic polarization (Fig. 5a), both Ru0-De and Ru2-De generate two potential-dependent bands in the 400–600 cm^{-1} region, which can reasonably be attributed to oxygen-containing intermediates associated with M–OH/M–OOH species. Compared with Ru0-De, these bands appear earlier in Ru2-De and shift significantly from approximately 477/549 cm^{-1} to about 465/539 cm^{-1}, indicating that the introduction of Ru facilitates the formation/evolution of OER intermediates and regulates the local environment of M–O bonds to enhance M–O covalency. Ru K-edge XAFS further supports this conclusion (Fig. 5b). The XANES spectra of Ru2-De before and after the HER/OER fall between those of Ru metal foil and RuO_2, with only slight changes after the OER, suggesting that Ru retains a stable partial oxidation state rather than evolving into a fully oxidized RuO_2-like phase. Meanwhile, FT-EXAFS analysis shows a retained first-shell Ru–O coordination feature but no metallic Ru–Ru contribution or higher-shell fingerprint characteristic of crystalline RuO_2 (Fig. 5c), indicating that the Ru species remain stabilized in a short-range ordered, long-range disordered amorphous Ru–O–P environment after the OER, rather than reconstructing into conventional crystalline RuO_2.

Density functional theory (DFT) calculations were performed to investigate the evolution of electronic structures and the origin of the enhanced structure stability. Considering the computational limitations on cell size, $Co_3(PO_4)_2$ and $Ni_3(PO_4)_2$ were selected as representative model systems to examine how Ru doping influences both structural and electronic properties. Moreover, given the limitations of current computational resources for direct modeling of complex multi-component amorphous systems, crystalline materials were employed as model systems. This simplification is based on the essential short-range order characteristic of amorphous materials. Experimental characterization confirms that although the Ru2-De surface layer lacks long-range periodicity, it retains uniform local coordination environments (Fig. 2), and the physicochemical properties of phosphate systems are primarily determined by the local coordination structures of metal–oxygen polyhedra and phosphate tetrahedra rather than long-range periodicity. Therefore, crystalline models can effectively capture the key electronic structure information of active sites. A negative E_{form} indicates thermodynamically favorable doping. As shown in Fig. S40, in the bulk phase, the formation energy

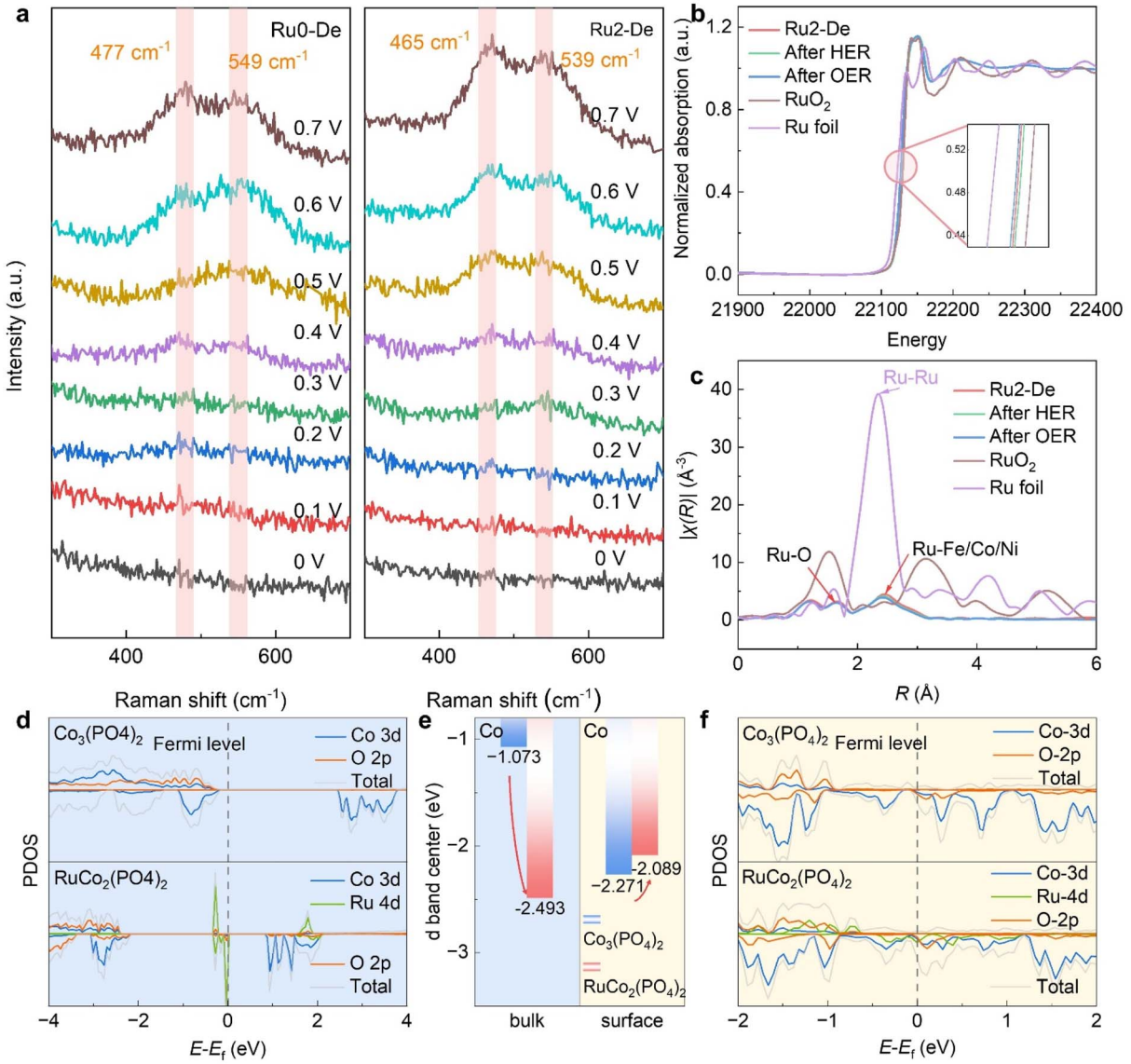

Fig. 5 (a) Changes in Ru0-De and Ru2-De Raman signals with increasing applied potential. (b) The normalized Pt K-edge XANES spectra of Ru foil, RuO_2, Ru2-De, after the HER and after the OER. (c) Fourier-transformed Ru K-edge EXAFS spectra of Ru2-De before and after electrocatalysis, along with Ru foil and RuO_2 references. PDOS of (d) the bulk and (f) surface of $Co_3(PO_4)_2$ and $RuCo_2(PO_4)_2$. (e) Comparison of the bulk and surface PDOS of $Co_3(PO_4)_2$ and the d-band center of Co before and after Ru doping.

for Ru substituting Ni is −1.98 eV, whereas that for Ru substituting Co is nearly thermoneutral (−0.05 eV), suggesting a stronger solubility preference of Ru at Ni sites. In contrast, for the surface systems, the formation energies for Ni- and Co-based phosphates are −0.47 eV and −0.463 eV, respectively, both significantly negative, indicating that surface sites of both materials can stably accommodate Ru.

Further projected density of states (PDOS) and d-band center analyses reveal the electronic origin of the doping effect. As shown in Fig. 5d–f and S41 in the undoped systems, the states near the Fermi level are primarily contributed by Ni/Co 3d orbitals with limited overlap with O 2p. Upon Ru incorporation, Ru 4d states contribute strongly near the Fermi level and exhibit enhanced hybridization with O 2p orbitals. This strengthened Ru–O hybridization reinforces the M–O covalency and thus suppresses phosphate anion dissolution. The d-band center analysis further indicates that, in the bulk phase, the Ni d-band shifts from −2.533 to −5.679 eV and the Co d-band shifts from −1.073 to −2.493 eV, both moving to lower energies and thereby stabilizing the electronic states. In contrast, at the surface, the Ni d-band shifts from −3.132 to −2.884 eV and the Co d-band shifts from −2.277 to −2.089 eV, moving closer to the Fermi level. This indicates that surface Ru not only provides highly active sites itself but also enhances the activity of adjacent Co sites. Overall, Ru doping provides structural stability in the bulk while simultaneously enhancing catalytic activity at the surface, thereby achieving a synergistic optimization of stability and catalytic performance.

Meanwhile, Ru doping significantly increases the density of states near the Fermi level and narrows the band gap, indicative of improved electronic conductivity. This trend is consistent with EIS measurements, where a lower charge-transfer resistance was observed, corroborating the promoted charge transport induced by doping. Moreover, phonon dispersion calculations (Fig. S42) show that no imaginary frequencies are observed throughout the Brillouin zone for both $RuNi_2(PO_4)_2$ and $RuCo_2(PO_4)_2$, confirming their dynamical stability. Collectively, these DFT results demonstrate that Ru doping, through multilevel synergistic regulation, enhances bulk structural stability while simultaneously activating surface sites, thereby providing a clear mechanistic rationale for achieving high activity and long-term durability of transition-metal phosphates under alkaline conditions.

Conclusions

In summary, this work presents a novel approach to address the long-standing stability issue of transition metal phosphate catalysts in electrochemical water splitting, by introducing trace amounts of ruthenium. We have developed an Ru2-De catalyst that exhibits outstanding HER and OER performance and retains stability for over 500 hours at 500 mA cm^{-2} in alkaline media. When used as the anode and cathode catalyst in an anion exchange membrane (AEM) electrolyzer, it can reach 500 mA cm^{-2} at a cell voltage of 1.61 V and retain stability for over 100 hours at 1000 mA cm^{-2}. The enhanced durability originates from the strengthened M–O bonding and suppressed phosphate group collapse due to Ru doping. DFT calculations further confirm that Ru doping enhances both structural stability and surface reactivity, achieving a synergistic optimization of performance and durability. The findings provide valuable insights into the design of next-generation, non-precious metal catalysts for large-scale hydrogen production.

Author contributions

Jinyan Xie: data curation, investigation, methodology, validation, writing-original draft; Shiyu Yang: data curation, writing-review & editing; Ziyong Zhang: data curation, methodology; Fei Han: supervision, validation, editing; Ruizhe Ru: data curation; Lei Zhang: data curation; Zunming Lu: data curation; Guowei Li: conceptualization, supervision, writing-review & editing; Jun-Qiang Wang: conceptualization, supervision, writing-review & editing, funding acquisition; Juntao Huo: conceptualization, supervision, writing-review & editing, funding acquisition.

Conflicts of interest

There are no conflicts to declare.

Data availability

The data supporting this article have been included as part of the supplementary information (SI).

Supplementary information: experimental section, Fig. S1–S42 and Tables S1–S5. See DOI: https://doi.org/10.1039/d6ta02016j.

Acknowledgements

We acknowledge financial support from the National Natural Science Foundation of China (NSFC U24A2039, 52471214, 52271016, and 52525105), the Zhejiang Provincial Natural Science Foundation of China under Grant (LRG26E010001), the Ningbo Yongjiang Talent Introduction Programme (2022A-090-G), and the International Cooperation Project of Ningbo City (2024H007).

Notes and references

1 L. Wang, X. Wang, H. Wang, C. Zhang, J. Li, G. Feng, X. Cheng, X. Qin, Z. Yu and T. Lu, *J. Am. Chem. Soc.*, 2025, **147**, 7555–7563.
2 Y. Fan, J. Zhao, J. Zhou, W.-H. Huang, J. Zhu, C. Kuo, S. Zhang, C. Pao, T. Chan, Y. Zhang, S. Hsu, J. Chen, C.-T. Chen, C. Jin, L. Tjeng, J. Wang, Z. Hu and L. Zhang, *Energy Environ. Sci.*, 2025, **18**, 7527–7540.
3 H. Chen, P. Liu, W. Li, W. Xu, Y. Wen, S. Zhang, L. Yi, Y. Dai, X. Chen, S. Dai, Z. Tian, L. Chen and Z. Lu, *Adv. Mater.*, 2024, **36**, 2411302.
4 Y. Zheng, C. Song, J. Zou, J. Fan, T. Wen and H. Wang, *Chem. Eng. J.*, 2025, **524**, 169189.
5 B. Kimmel, T. Morawietz, P. Gazdzicki, A. S. Gago and K. A. Friedrich, *Electrochim. Acta*, 2025, **542**, 147395.
6 B. Chang, X. Liu, S. Zuo, Y. Ren, J. He, D. Wang, Y. Lei, M. Hu, W.-L. Li, M. A. Khan, R. Aleisa, R. Hu, Y. Hou, H. Liu, W. Zhou, Z. Lai, H. N. Alshareef and H. Zhang, *Nat. Commun.*, 2025, **16**, 7959.
7 J. Zhao, R. Urrego-Ortiz, N. Liao, F. Calle-Vallejo and J. Luo, *Nat. Commun.*, 2024, **15**, 6391.
8 Z. Li, G. Lin, L. Wang, H. Lee, J. Du, T. Tang, G. Ding, R. Ren, W. Li, X. Cao, S. Ding, W. Ye, W. Yang and L. Sun, *Nat. Catal.*, 2024, **7**, 944–952.
9 M. Ning, S. Wang, J. Wan, Z. Xi, Q. Chen, Y. Sun, H. Li, T. Ma and H. Jin, *Angew. Chem., Int. Ed.*, 2024, **63**, e202415794.
10 W. Li, D. Chen, Z. Lou, H. Yuan, X. Fu, H. Y. Lin, M. Lin, Y. Hou, H. Qi, P. F. Liu, H. G. Yang and H. Wang, *J. Am. Chem. Soc.*, 2025, **147**, 10446–10458.
11 X. Y. Zhang, H. Yin, C. C. Dang, H. Nie, Z. X. Huang, S. H. Zheng, M. Du, Z. Y. Gu, J. M. Cao and X. L. Wu, *Angew. Chem., Int. Ed.*, 2025, **64**, e202425569.
12 X. Wang, H. Jang, S. Liu, Z. Li, X. Zhao, Y. Chen, M. G. Kim, Q. Qin and X. Liu, *Adv. Energy Mater.*, 2023, **13**, 2301673.
13 Q. Yang, Y. Zhang, Y. Sun, C. Felser and G. Li, *Innovation Mater.*, 2023, **1**, 100013.
14 Y. Ma, K. Siuzdak and G. Li, *Innovation Mater.*, 2025, **3**, 100157.
15 L. Zong, F. Lu, P. Li, K. Fan, T. Zhan, P. Liu, L. Jiang, D. Chen, R. Zhang and L. Wang, *Adv. Mater.*, 2024, **36**, 2403525.
16 T. Wen, Y. Zheng, J. Zou and H. Wang, *J. Mater. Chem. A*, 2026, **14**, 9138–9176.

17 N. Stegmann, H. Petersen, C. Weidenthaler and W. Schmidt, *J. Mater. Chem. A*, 2021, **9**, 18247–18250.
18 S. Liu, Y. Zhang, W. Sun, J. Wang, D. Zhang, J. Huo and G. Li, *Chem. Commun.*, 2025, **61**, 3669–3672.
19 S. Yang, K. Yue, X. Liu, S. Li, H. Zheng, Y. Yan, R. Cao and W. Zhang, *Nat. Commun.*, 2024, **15**, 1410.
20 P. Tian, W. Zong, J. Xiong, W. Liu, J. Liu, Y. Dai, J. Zhu, S. Huang, S. Song, K. Chu, G. He and N. Han, *Adv. Funct. Mater.*, 2025, **35**, 2504862.
21 K. Song, H. Zhang, Z. Lin, Z. Wang, L. Zhang, X. Shi, S. Shen, S. Chen and W. Zhong, *Adv. Funct. Mater.*, 2023, **34**, 2312672.
22 T. Xu, J. Yu, J. Ma, H. Yu, J. Che, Q. Yin, Y. Xi, Y. Cao, M. Shi, S. Wang, W. Wan, C. Li, R. Chen, J. Zhang, Q. Zhao, W. Ren, M. Hu and X. Li, *Energy Environ. Mater.*, 2025, **8**, e70043.
23 R. P. Darminto, M. A. Nuruzzahran, D. A. Syaifullah, H. Ilhami, N. N. Mobarak, H. AlMohamadi, F. Fathurrahman, N. L. W. Septiani and A. G. Saputro, *Langmuir*, 2025, **41**, 10205–10215.
24 J. Kwon, H. Han, S. Jo, S. Choi, K. Y. Chung, G. Ali, K. Park, U. Paik and T. Song, *Adv. Energy Mater.*, 2021, **11**, 2100624.
25 X. Li and J. Wang, *Adv. Mater. Interfaces*, 2020, **7**, 2000676.
26 J. Fan, C. Song, Y. Zhang, H. Wang and J. Zou, *Appl. Catal. B-Environ. Energy*, 2026, **385**, 126268.
27 T. Wen, Y. Zheng, H. Wang and J. Zou, *Appl. Catal. B-Environ. Energy*, 2025, **378**, 125588.
28 T. Wen, M. Yang, J. Zou and H. Wang, *Ind. Eng. Chem. Res.*, 2025, **64**, 9209–9216.
29 X. Li, T. Wen, Y. Zheng, J. Zou and H. Wang, *J. Power Sources*, 2025, **653**, 237772.
30 Y. Li, Z. Dong and L. Jiao, *Adv. Energy Mater.*, 2019, **10**, 1902104.
31 Z. Pu, T. Liu, I. S. Amiinu, R. Cheng, P. Wang, C. Zhang, P. Ji, W. Hu, J. Liu and S. Mu, *Adv. Funct. Mater.*, 2020, **30**, 2004009.
32 P. Ye, K. Fang, H. Wang, Y. Wang, H. Huang, C. Mo, J. Ning and Y. Hu, *Nat. Commun.*, 2024, **15**, 1012.
33 S. Li, L. Wang, H. Su, A. N. Hong, Y. Wang, H. Yang, L. Ge, W. Song, J. Liu, T. Ma, X. Bu and P. Feng, *Adv. Funct. Mater.*, 2022, **32**, 2200733.
34 D. Shakhvorostov, M. H. Müser, N. J. Mosey, Y. Song and P. R. Norton, *Phys. Rev. B:Condens. Matter Mater. Phys.*, 2009, **79**, 094107.
35 C. Rong, K. Dastafkan, Y. Wang and C. Zhao, *Adv. Mater.*, 2023, **35**, 2211884.
36 L. Wang, Z. Li, H. Jang, M. G. Kim, S. Liu, X. Wang, M. Zeng, J. Cho, X. Liu and Q. Qin, *Adv. Funct. Mater.*, 2024, **35**, 2421615.
37 S. Jiang, L. Zhu, Z. Yang and Y. Wang, *Electrochim. Acta*, 2021, **368**, 137618.
38 T. Zhang, X. Ren, S. Mo, W. Cao, C. Zhou, F. Ma, R. Chen, C. Zeng, L. Shi, T. Liu, H. Zhang and H. Ni, *J. Mater. Sci. Technol.*, 2024, **199**, 66–74.
39 J. Q. Wang, L. J. Song, J. T. Huo, M. Gao and Y. Zhang, *Adv. Mater.*, 2024, **36**, 2311406.
40 J. Zhou, F. Qiao, Z. Ren, X. Hou, Z. Chen, S. Dai, G. Su, Z. Cao, H. Jiang and M. Huang, *Adv. Funct. Mater.*, 2023, **34**, 2304380.
41 Z. Yu, S. Lv, Q. Yao, N. Fang, Y. Xu, Q. Shao, C. W. Pao, J. F. Lee, G. Li, L. M. Yang and X. Huang, *Adv. Mater.*, 2022, **35**, 2208101.
42 M. Pan, H. Feng, Z. Zhang, M. Gao, L. Lei, D. Wang, G. Li, J. Huo and J.-Q. Wang, *J. Mater. Chem. A*, 2024, **12**, 15334–15342.
43 C. Guan, X. Yue and Q. Xiang, *Adv. Mater.*, 2025, **37**, 2501209.
44 H. Meng, Z. Chen, J. Zhu, B. You, T. Ma, W. Wei, S. Vernuccio, J. Xu and B. J. Ni, *Adv. Funct. Mater.*, 2024, **34**, 2405270.
45 Y. Zhang, Y. Wang, W. Sun, D. Ma, J. Ma, J. Rao, Q. Xu, J. Huo, J. Liu and G. Li, *Adv. Mater. Interfaces*, 2023, **10**, 2300279.
46 L.-M. Cao, J. Zhang, L.-W. Ding, Z.-Y. Du and C.-T. He, *J. Energy Chem.*, 2022, **68**, 494–520.
47 E. Fabbri, M. Nachtegaal, T. Binninger, X. Cheng, B.-J. Kim, J. Durst, F. Bozza, T. Graule, R. Schäublin, L. Wiles, M. Pertoso, N. Danilovic, K. E. Ayers and T. J. Schmidt, *Nat. Mater.*, 2017, **16**, 925–931.
48 X. Liu, S. Wei, S. Cao, Y. Zhang, W. Xue, Y. Wang, G. Liu and J. Li, *Adv. Mater.*, 2024, **36**, 2405970.
49 M. Görlin, J. Ferreira de Araújo, H. Schmies, D. Bernsmeier, S. Dresp, M. Gliech, Z. Jusys, P. Chernev, R. Kraehnert, H. Dau and P. Strasser, *J. Am. Chem. Soc.*, 2017, **139**, 2070–2082.
50 A. S. Disa, T. F. Nova and A. Cavalleri, *Nat. Phys.*, 2021, **17**, 1087–1092.
51 Z. Xu, J. Zhu, J. Shao, Y. Xia, P. Liu, G. Li, R. Chen, S. Chen, J. Wang, S. Chen, F. Huang and H.-L. Wang, *Energy Environ. Sci.*, 2024, **17**, 8722–8733.
52 Y. Zhang, Z. Li, H. Jang, M. G. Kim, J. Cho, S. Liu, X. Liu and Q. Qin, *Adv. Mater.*, 2025, **37**, 2501586.
53 X. Sun, Y. Liu, D. Zheng, C. Qin, Z. Wang and H. Wang, *Corros. Sci.*, 2024, **235**, 112225.
54 G. Li, Q. Yang, J. Rao, C. Fu, S. C. Liou, G. Auffermann, Y. Sun and C. Felser, *Adv. Funct. Mater.*, 2020, **30**, 1907791.
55 D. Wu and J. Luo, *Quantum Front.*, 2023, **2**, 13.
56 C. Wang, P. Zou, W. Xu, Y. Zhang, J. Huo, J.-Q. Wang, Y. Liu and C. Qin, *J. Alloys Compd.*, 2024, **995**, 174790.
57 Z. Yu, Y. Li, V. Martin-Diaconescu, L. Simonelli, J. Ruiz Esquius, I. Amorim, A. Araujo, L. Meng, J. L. Faria and L. Liu, *Adv. Funct. Mater.*, 2022, **32**, 2206138.
58 Z. Yu, D. W. Boukhvalov, H. Tan, D. Xiong, C. Feng, J. Wang, W. Wang, Y. Zhao, K. Xu, W. Su, X. Xiang, F. Lin, H. Huang, F. Zhang, L. Zhang, L. Meng and L. Liu, *Chem. Eng. J.*, 2024, **494**, 153094.

